applied sciences

MDPI

Article

Influence of Fin Spacing and Fin Height in Passive Heat Sinks: Numerical Analysis with Experimental Comparison

Mateo Kirinčić *, Tin Fadiga and Boris Delač

Faculty of Engineering, University of Rijeka, Vukovarska 58, 51000 Rijeka, Croatia; fadiga.tin1997@gmail.com (T.F.); boris.delac@riteh.uniri.hr (B.D.)
* Correspondence: mateo.kirincic@riteh.uniri.hr

Abstract

In this paper, heat dissipation through a passive vertical plate fin heat sink via natural convection was numerically investigated. The influence of two nondimensional geometric parameters, fin spacing-to-thickness ratio and fin height-to-spacing ratio, on the heat sink's thermal performance was evaluated. A mathematical model describing the three-dimensional steady-state problem of buoyancy-driven flow and heat transfer was formulated. The solution was obtained numerically using the finite volume method in Ansys Fluent. The model and numerical procedure were validated by comparing the numerical predictions with measurements acquired on a constructed experimental apparatus. The heat sink thermal performance was assessed based on a series of performance metrics: heat dissipation rate, heat transfer coefficient, overall thermal resistance, and fin efficiency. Fin spacing-to-thickness ratio was varied between 1.86 and 4.8. Heat dissipation rate displayed a clear peak at a value of approximately 2.6, which coincided with a minimum in the overall thermal resistance. The heat transfer coefficient initially grew steadily, but at higher values of fin spacing-to-thickness ratio, it began to stagnate. Fin efficiency consistently decreased across the investigated range. Fin height-to-spacing ratio was varied between 1.11 and 7.78. The heat dissipation rate increased almost linearly across this range, but when the mass-specific heat dissipation rate was considered, it yielded diminishing returns. The heat transfer coefficient likewise exhibited a plateauing trend, while fin efficiency decreased steadily across the investigated range of fin height-to-spacing ratio. The obtained numerical results provide guidelines for geometry selection and can serve as a foundation for further analyses and optimizations of passive heat sinks' thermal performance.

Keywords: passive vertical heat sink; geometric parameters; fin spacing; fin height; numerical analysis; experimental validation

check for updates

Academic Editor: José A. Orosa García

Received: 8 October 2025
Revised: 20 October 2025
Accepted: 21 October 2025
Published: 24 October 2025

Citation: Kirinčić, M.; Fadiga, T.; Delač, B. Influence of Fin Spacing and Fin Height in Passive Heat Sinks: Numerical Analysis with Experimental Comparison. *Appl. Sci.* **2025**, *15*, 11410. https://doi.org/10.3390/app152111410

Copyright: © 2025 by the authors. Licensee MDPI, Basel, Switzerland. This article is an open access article distributed under the terms and conditions of the Creative Commons Attribution (CC BY) license (https://creativecommons.org/licenses/by/4.0/).

1. Introduction

Passive heat sinks are widely used in electronics and broader energy/industrial systems where quiet, reliable operation is desirable. In passive designs, heat is removed mainly by natural convection, with radiation sometimes contributing. Performance depends on material, geometry and surface characteristics, and the chosen cooling mode [1,2].

The theoretical foundations for natural convection between parallel surfaces were established in 1942 by Elenbaas [3], who developed the analytical framework for buoyancy-driven flows. Building on this, Bar-Cohen and Rohsenow [4] developed a semi-analytical model to determine thermally optimum fin spacing for maximum heat dissipation under natural convection. They demonstrated that fins spaced too closely restrict airflow and

suppress buoyancy effects, while overly wide spacing underutilizes surface area. This optimum spacing principle remains central to design methodology and is widely cited in subsequent works.

The influence of geometry has been extensively studied. Meng et al. [5] numerically investigated the effect of mounting angle on a straight fin heat sink under natural convection, reporting maximum cooling at 90° and a performance drop at 15° due to a heat transfer stagnation zone in the heat sink channels. They identified a heat transfer stagnation zone as the main factor that affects the cooling power of the heat sink, and its location and area vary with the mounting angle. Similarly, Shen et al. [6] experimentally and numerically examined eight orientations of rectangular plate fin heat sinks for LED cooling, showing strong orientation effects: 270°, i.e., horizontal fins, perform the worst due to plume blockage, while 45° and 135° deliver the highest heat transfer performance, with 315° being slightly lower. They also observed that orientation sensitivity decreases with increasing fin spacing.

Bar-Cohen et al. [7] performed a detailed computational study of arrays on an isothermal base plate, varying fin spacing, fin thickness, height, length, and base-to-ambient temperature difference. They evaluated the overall heat transfer coefficient and identified the best-performing geometry parameters.

Mehrtash and Tari [8] numerically investigated natural convection heat transfer from inclined plate-finned heat sinks using a validated numerical model. By varying the gravitational vector, they studied inclination effects across angles from $-60°$ to 90°. The study covered a wide Rayleigh number range (up to 2×10^8) and proposed a generalized correlation for predicting convective heat transfer rates in rectangular plate-fin arrays under different inclinations.

Jeon and Byon [9] numerically analyzed dual height plate fin heat sinks under natural convection, analyzing fin spacing and channel length. They showed that lowering the secondary fin height degrades total thermal performance, while performance per unit mass can increase.

Huang et al. [10] numerically studied a heat pipe heat sink with a variable height plate fin array under natural convection using 3D CFD and multi-objective optimization. Their results show that variable heights lower flow resistance and improve performance, highlighting the need to balance surface area with flow accessibility.

Fuse et al. [11] experimentally evaluated die-cast aluminum heat sinks under natural convection and radiation, varying heat sink material, fin height (20–35 mm), and base thickness (2–6 mm), with and without blackening. They observed that in both as-cast, i.e., non-blackened, and blackened heat sinks, the taller fins and thicker bases enhance dissipation, although the benefit of base thickening wanes at larger fin heights.

Abbas and Wang [12] proposed a displacement design for plate fin heat sinks in natural convection, where alternate fins are offset. Using experiments and numerical simulations, they varied fin spacing, length, height, and heat flux. It was observed that displacement delays boundary layer merging and entrains outside air near the channel exit, yielding the largest gains at small spacings but tending to hinder performance at very wide spacings. Furthermore, the authors noted that increasing fin length noticeably improved cooling; increasing fin height had a minor effect, while varying thermal load, but overall it had a largely negligible effect on which design performed best. Reported improvements include up to 56% lower thermal resistance and, at fixed volume, approximately 30% higher heat transfer with 28.7% less mass and 27.4% less area than a conventional design.

Using a validated heat transfer correlation for pin fins and established correlations for plate fins, Joo and Kim [13] optimized both heat sinks for a given base-to-ambient temperature difference and identical base dimensions and fin heights. Two objectives were

defined: total heat removal and removed heat per unit mass. Plate fins exhibited superior performance in total heat removal, while pin fins dominated in heat removal per unit mass, offering lighter designs with higher specific performance.

Ahmadi et al. [14] conducted a combined numerical–experimental study examining steady natural convection from vertically mounted rectangular interrupted fins. Using a 2D model and a custom testbed with 12 aluminum heat sinks, the parametric analysis (fin spacing, interruption) showed that interruptions significantly enhance performance and exhibit an optimum length.

Quintino et al. [15] numerically mapped natural convection from two vertical plates, varying Rayleigh number, dimensionless horizontal spacing, and dimensionless vertical alignment. They determined a Rayleigh number and alignment-dependent optimal spacing that maximizes total Nusselt; the optimum shrinks as the Rayleigh number rises and as the plates approach face-to-face. At large gaps, the plates behave independently, i.e., at intermediate gaps, reduced stagger strengthens the chimney effect, while at very tight gaps, more stagger improves exposure.

McCay et al. [16] numerically optimized natural convection heat sinks, validating against semi-empirical correlations and the literature. After spacing optimization of a rectangular baseline, they compared rectangular, trapezoidal, curved, and angled fins under equal surface area constraints. A curved fin with a shroud performed best, lowering system thermal resistance by 4.1% and raising the heat transfer coefficient by 4.4%.

Many other types of heat sink fin geometries have also been investigated. More complex types, such as sinusoidal wavy fins [17], dimpled fins [18], interrupted, staggered, and capped fins [19], and perforated fins [20], as well as cross-fin heat sinks [21] and shark skin-inspired biomimetic designs [22], are also reported in the literature. Even though complex geometries have shown performance gains in some contexts, their manufacturing complexity and cost can be prohibitive.

Conventional plate fin geometry still shows strong spacing/fin number trade-offs, with recent CFD maps indicating that changing only the number of fins and fin spacing can enhance the heat dissipation rate while also reducing metal usage and footprint at the cost of higher hydraulic resistance as spacing narrows [23]. These results underscore that performance is governed by how added surface area competes with buoyancy-limited flow access, which motivates parameterizing geometry with compact, transferable ratios. Using a three-dimensional natural convection model of a horizontal straight-fin heat sink, Huang and Chen [24] showed that fin height and longitudinal displacement are decisive design variables; the optimization reduced base temperature and thermal resistance, with fin spacing emerging as especially influential. Muneeshwaran et al. [25] found that a notched fin concept for horizontal natural convection heat sinks achieved sizable thermal resistance reductions and identified practical optima (notch length and fin spacing), illustrating that slot openness can be more valuable than raw surface area, especially when radiation/emissivity is also considered.

Collectively, prior work converges on the observation that geometric parameters, particularly fin spacing, followed by fin height and thickness, significantly affect natural convection performance in vertical plate fin heat sinks. Despite extensive work on natural convection heat sinks, recent studies still report performance shifts driven by geometry choices (spacing, fin number, thickness profiles) but typically present results in dimensional terms that are not easily transferable across designs. To address this, this study introduces two dimensionless geometry ratios, fin spacing-to-thickness ratio (S^*) and fin height-to-spacing ratio (H^*), and maps heat sink performance—heat dissipation rate (including mass-specific metrics), heat transfer coefficient, overall thermal resistance, and fin efficiency—over the investigated S^* and H^* ranges. The mass-aware perspective is included to expose

weight/material trade-offs at a fixed footprint; because heat sink mass increases with fin height and fin number, the mass-specific heat dissipation rate highlights where added geometry yields diminishing returns relative to added material, as indicated by previous studies [13,26,27]. The analysis is supported by a calorimetry-based experiment and an experimentally validated numerical model under buoyancy-driven convection, providing generalizable design guidance at fixed base area and clarifying the trade-off between added surface and flow access.

2. Mathematical Modeling and Numerical Solving

2.1. Problem Formulation and Domain Selection

In passive heat sinks, the heat produced by an electronic component is first conducted into the heat sink base, from where it spreads both laterally and upward through the array of fins. Heat is carried along each fin from its root toward the tip, creating a temperature gradient along the fin length. At the fin surfaces, the thermal energy is dissipated to the surrounding air by natural convection. This process is driven by buoyancy, as the warmer air near the fins rises and is replaced by cooler ambient air.

In this work, a solid, vertically oriented aluminum passive heat sink attached to a heat-generating component and operating in undisturbed air was examined (Figure 1). The heat sink employed was a commercially available extruded aluminum model with straight, vertical plate fins. No surface treatments were applied, and all surfaces remained bare aluminum. The geometric details of the baseline heat sink configuration are summarized in Table 1.

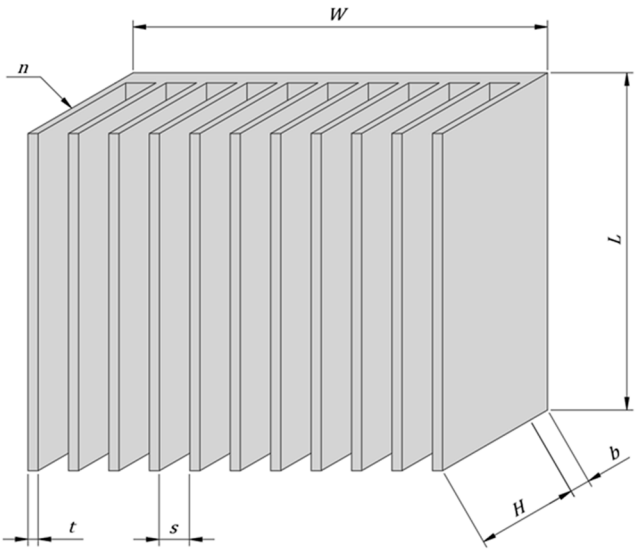


Figure 1. Examined heat sink configuration with denoted geometric parameter symbols.

Table 1. Geometric specifications of the baseline heat sink configuration.

Geometric Parameter	Value
Overall width (W, mm)	123
Overall length; fin length (L, mm)	100
Base thickness (b, mm)	6
Fin number (n, –)	11
Fin height (H, mm)	30
Fin spacing (s, mm)	9
Fin thickness (t, mm)	3

The baseline heat sink configuration was chosen as a commercially available extruded plate fin unit, representative of standard passive coolers and matching the experiment. The base area keeps a compact aspect ratio; fin thickness was set to 3 mm, a typical extrusion value that also supports robust meshing. A polished, untreated aluminum surface was used to align the experiment with the model by minimizing radiation. The selected fin number and fin spacing are both near the center of the analyzed design space, avoiding extremes where the slots are either choked or overly sparse. This mid-range baseline is consistent with conventional parallel plate guidance, which predicts an intermediate optimum spacing under natural convection; it also provides a neutral reference for symmetric excursions above and below in the parametric study.

In addition, the vertical orientation was adopted because, under natural convection, this configuration promotes a chimney-type flow in the slots between the fins, thus yielding higher total heat dissipation and average heat transfer coefficients than horizontal, gravity-perpendicular channels. This trend has been demonstrated across orientation and inclination studies and provides a physically favorable, widely manufactured baseline for validation and parametric mapping [6,8].

The heat sink's geometry is symmetric in both width and length directions, but because natural convection effects act in the vertical direction, the problem itself is physically symmetric only in the width direction. Therefore, one half of the heat sink's width ($W/2$) is sufficient to consider for numerical treatment as it captures all physical phenomena of the analyzed problem. This approach cuts the computational cost significantly without sacrificing accuracy.

In order to adequately capture the natural convection behavior in the immediate proximity of the heat sink, an air region surrounding it was defined. In the y direction, it spans 100 mm (L) below the bottom and 100 mm (L) above the top of the heat sink. In the x direction, it spans 30 mm (H) from the edge of the heat sink. In the z direction, it spans 90 mm ($3H$) from the fin tips (front of the heat sink) and an additional 30 mm (H) from the base to the back. However, the latter does not include the region behind the heat sink base, as that is where the heat sink is in contact with the electronic component. The thusly defined computational domain, shown in Figure 2, comprises two subdomains: aluminum heat sink and air.

The analyzed case is a steady-state conjugate heat transfer problem, where conduction occurs within the aluminum heat sink while natural convection develops in the surrounding air. The thermophysical properties of air, evaluated at the film temperature of 40 °C (the arithmetic mean of the heat sink surface and ambient air temperatures), and aluminum are listed in Table 2.

Table 2. Thermophysical properties of aluminum and air.

Thermophysical Property	Al	Air
Thermal expansion coefficient (β, 1/K)	–	0.0032
Density (ρ, kg/m^3)	2719	1.13
Thermal conductivity (k, W/(m·K))	202.4	0.0267
Specific heat capacity (c_p, J/(kg·K))	381	1007
Dynamic viscosity (μ, Pa·s)	–	1.872×10^{-5}

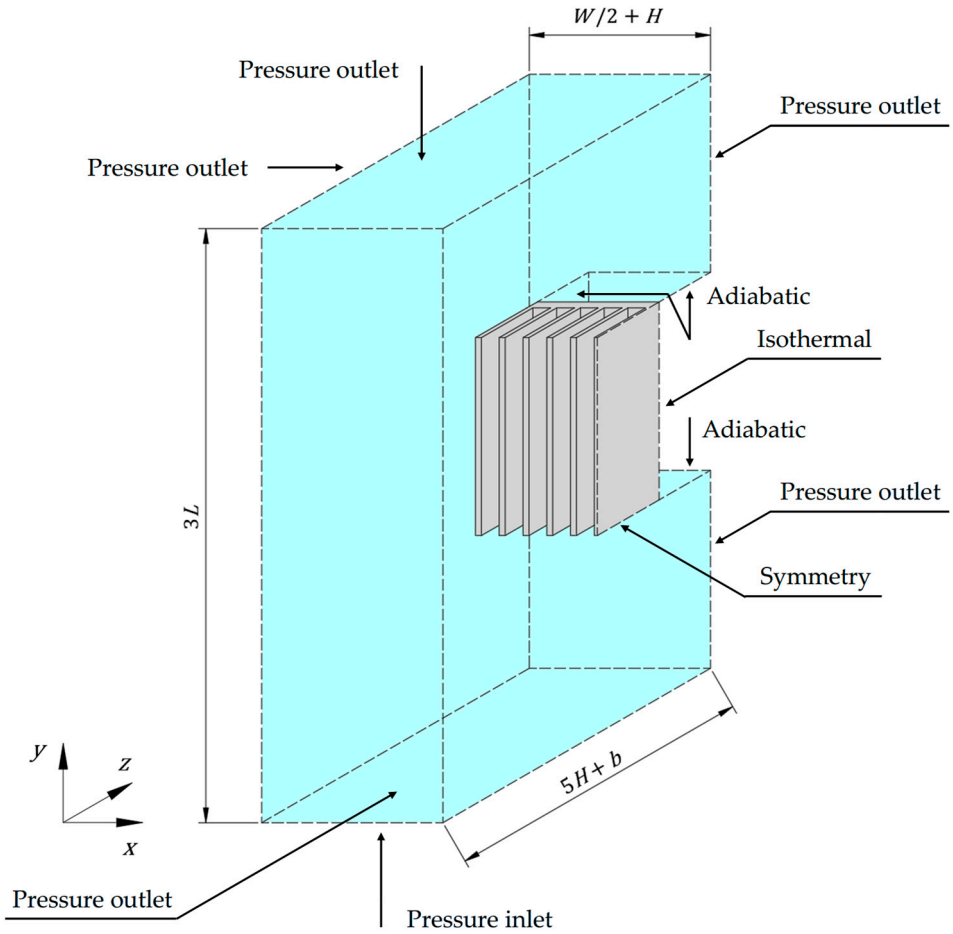


Figure 2. Schematic of the computational domain and applied boundary conditions.

2.2. Model Assumptions and Justification

The problem is analyzed as three-dimensional because the heat sink is a finite array, not an infinite parallel plate channel. End and tip effects create spanwise pressure gradients and corner plumes at the array outlet, fin tips and base edges exchange heat on multiple faces, and lateral bypass along the outermost channels alters the local velocity and temperature fields. In addition, thermal spreading in the base occurs in both the streamwise and spanwise directions, and the fin temperature is non-uniform along the height and width.

The problem is considered steady-state because many electronic components operate at an approximately constant heat dissipation rate. The performed calorimetry experiments were designed, and the validation data extracted, to correspond to a quasi-steady window in which base temperature and heat flux transients were considered negligible.

To determine the flow regime, the vertical plate Rayleigh number is evaluated:

$$\mathrm{Ra_L} = \frac{g\beta_{\mathrm{air}}\rho_{\mathrm{air}}^2 c_{\mathrm{p,air}}\left(\overline{T}_S - T_{\mathrm{air}}\right)L^3}{\mu_{\mathrm{air}}k_{\mathrm{air}}} \quad (1)$$

Inputting the values of the thermophysical properties of air given in Table 2, the fin length L provided in Table 1, and the heat sink surface and ambient temperatures ($\overline{T_S}$ and T_{air}, respectively) used in the present investigation gives the value of $\mathrm{Ra_L}$ in the range 1.13×10^6 and 2.5×10^6. This is below the transition band (order of magnitude 10^9), indicating laminar natural convection.

Natural convection was assumed to be driven only by buoyancy forces, with density variations introduced through the incompressible ideal gas law. Characteristic velocities in

natural convection over centimeter-scale fins are reasonably small, with a Mach number significantly below the value of 0.3 where compressibility effects would be noticeable. All other fluid properties were treated as constant and evaluated at the film temperature, a standard in natural convection modeling.

Effects of viscous dissipation are negligible at present velocities as the Eckert number is significantly below 1.

Radiative heat transfer is also neglected, as Aihara et al. [28] report that in heat sinks with a low emissivity surface, radiation makes for about 5% or less of the total heat transfer, which can be considered negligible.

The mid-width symmetry plane was modeled as adiabatic and impermeable. Because the geometry and physical phenomena are symmetric with respect to the mid-plane, a symmetry boundary reduces cost without biasing results.

The heat sink base was prescribed a uniform temperature. An isothermal base boundary condition was chosen because aluminum's high thermal conductivity rapidly equalizes in-plane temperature across the base. In practice, as well as in the validation setup, the base–source interface is tightened with thermal paste to minimize contact resistance and further uniformize the boundary condition. Accordingly, the measured base temperature varied only slightly over the measurement interval used for validation.

Finally, the ambient air temperature at locations sufficiently distant from the heat sink was taken to be constant. The external domain boundaries are placed sufficiently far from the heat sink so that enlarging the domain further would have no significant effect on the thermal performance metrics.

2.3. Conservation Equations

For the analyzed physical problem, conservation equations of mass and momentum are applied for the fluid (air) subdomain, while the energy conservation equation is applied to both the solid (aluminum) and fluid subdomains. The equations are as follows:

- Conservation of energy (solid):

$$\frac{\partial^2 T}{\partial x^2} + \frac{\partial^2 T}{\partial y^2} + \frac{\partial^2 T}{\partial z^2} = 0 \tag{2}$$

- Conservation of mass (fluid):

$$\frac{\partial(\rho_{\text{air}} w_x)}{\partial x} + \frac{\partial(\rho_{\text{air}} w_y)}{\partial y} + \frac{\partial(\rho_{\text{air}} w_z)}{\partial z} = 0 \tag{3}$$

- Conservation of momentum—x direction (fluid):

$$\rho_{\text{air}}\left(w_x \frac{\partial w_x}{\partial x} + w_y \frac{\partial w_x}{\partial y} + w_z \frac{\partial w_x}{\partial z}\right) = -\frac{\partial p}{\partial x} + \mu_{\text{air}}\left(\frac{\partial^2 w_x}{\partial x^2} + \frac{\partial^2 w_x}{\partial y^2} + \frac{\partial^2 w_x}{\partial z^2}\right) \tag{4}$$

- Conservation of momentum—y direction (fluid):

$$\rho_{\text{air}}\left(w_x \frac{\partial w_y}{\partial x} + w_y \frac{\partial w_y}{\partial y} + w_z \frac{\partial w_y}{\partial z}\right) = -\frac{\partial p}{\partial y} + \mu_{\text{air}}\left(\frac{\partial^2 w_y}{\partial x^2} + \frac{\partial^2 w_y}{\partial y^2} + \frac{\partial^2 w_y}{\partial z^2}\right) + \rho_{\text{air}} g_y \tag{5}$$

- Conservation of momentum—z direction (fluid):

$$\rho_{\text{air}}\left(w_x \frac{\partial w_z}{\partial x} + w_y \frac{\partial w_z}{\partial y} + w_z \frac{\partial w_z}{\partial z}\right) = -\frac{\partial p}{\partial z} + \mu_{\text{air}}\left(\frac{\partial^2 w_z}{\partial x^2} + \frac{\partial^2 w_z}{\partial y^2} + \frac{\partial^2 w_z}{\partial z^2}\right) \tag{6}$$

- Conservation of energy (fluid):

$$\rho_{\text{air}}\left(w_x\frac{\partial T}{\partial x}+w_y\frac{\partial T}{\partial y}+w_z\frac{\partial T}{\partial z}\right)=\frac{k_{\text{air}}}{c_{\text{p,air}}}\left(\frac{\partial^2 T}{\partial x^2}+\frac{\partial^2 T}{\partial y^2}+\frac{\partial^2 T}{\partial z^2}\right) \tag{7}$$

Within the incompressible ideal gas law framework, buoyancy-induced density variation is accounted for without the need to solve the fully compressible continuity and momentum equations. An operating pressure (p_{op}), typically taken as atmospheric pressure, is specified, while the local fluid density is determined from the ideal gas Equation [29]:

$$\rho=\frac{p_{\text{op}}}{RT} \tag{8}$$

In Equation (8), R denotes the specific gas constant (J/(kg·K)). The density field is incorporated into the continuity equation, ensuring mass conservation even under variable density conditions. In the y-momentum equation, the buoyancy source term generates an upward force in regions where the fluid is warmer and therefore lighter. This density formulation is particularly appropriate for larger temperature differences between the heat source and the ambient air, which enables analyses over a broader range of ambient and heat sink operating conditions than other commonly used density formulations, e.g., the Boussinesq approximation.

2.4. Boundary Conditions

Boundary conditions were defined at the boundaries of the computational domain (as indicated in Figure 2) as well as at the solid–fluid interface between the heat sink and surrounding air.

At the bottom boundary of the domain, a pressure inlet condition was applied, defining atmospheric pressure with flow directed normally to the surface. The temperature at this boundary was fixed to the ambient value. It can be written as follows:

$$p=p_\infty \tag{9}$$

$$T=T_\infty \tag{10}$$

For the lateral, front, top, upper rear, and bottom rear boundaries, pressure outlet conditions were imposed. Atmospheric pressure was specified, while any potential backflow was constrained to follow the direction of the neighboring interior cells, with the backflow temperature set equal to the ambient temperature. This can be expressed as:

$$p=p_\infty \tag{11}$$

$$T=T_\infty \tag{12}$$

At pressure inlet and pressure outlet boundaries, the pressure value is fixed, as opposed to velocity-specified boundaries. Here, velocity is calculated so that it ensures continuity with both the outlet conditions and the internal flow field.

Adiabatic wall and no-slip conditions were applied on the recess behind the heat sink's upper and lower horizontal and rear vertical boundaries. This boundary condition can be formulated as:

$$\frac{\partial T}{\partial n}=0 \tag{13}$$

$$w_x=0 \tag{14}$$

$$w_y=0 \tag{15}$$

$$w_z = 0 \tag{16}$$

At the heat sink base, an isothermal boundary condition is prescribed, i.e.,:

$$T = T_b \tag{17}$$

At the symmetry plane, a symmetry boundary condition is applied. This assumes that no flow or heat transfer occurs normal to the plane and that all variables exhibit zero gradient in the direction perpendicular to it. For both the solid and fluid regions, this means:

$$\frac{\partial T}{\partial x} = 0 \tag{18}$$

For the fluid subdomain, the following additional constraints are imposed:

$$w_x = 0 \tag{19}$$

$$\frac{\partial w_y}{\partial x} = 0 \tag{20}$$

$$\frac{\partial w_z}{\partial x} = 0 \tag{21}$$

Finally, at the interface between the solid and the fluid, conductive boundary layer heat transfer is defined, together with the no-slip condition:

$$k_{Al}\frac{\partial T}{\partial n} = k_{air}\frac{\partial T}{\partial n} \tag{22}$$

$$w_x = 0 \tag{23}$$

$$w_y = 0 \tag{24}$$

$$w_z = 0 \tag{25}$$

2.5. Numerical Solving

The numerical solution was obtained using the finite volume method [30], with simulations performed in the Ansys Fluent 18.2 solver. Pressure–velocity coupling was handled with the SIMPLE algorithm, ensuring that density was treated solely as a function of temperature rather than being affected by local pressure variations. For pressure discretization, the PRESTO! scheme was employed, while convective terms in both the momentum and energy equations were discretized with the second-order upwind scheme. To improve aid convergence, the incompressible ideal gas formulation was stabilized by prescribing an operating density corresponding to the ambient temperature. Furthermore, under-relaxation factors of 0.3, 0.6, and 1 were applied to the pressure, momentum, and energy equations, respectively. Convergence was considered achieved once residuals dropped below 10^{-3} for continuity and 10^{-6} for both momentum and energy.

For a base temperature of 50 °C and ambient temperature of 29 °C, a mesh independence study was performed by evaluating a series of numerically obtained parameters: heat dissipation rate $\dot{Q}$, heat transfer coefficient h, and average temperature at the heat sink surface $\overline{T_S}$ across four different mesh sizes: 525,900 (M1), 1,220,204 (M2), 4,119,600 (M3), and 8,968,725 cells (M4). A mesh refinement study for all three observed quantities is shown in Table 3, along with percent changes relative to the next finer mesh (for $\dot{Q}$ and h) and absolute temperature change for $\overline{T_S}$. For each refinement step, the percent change of a quantity (δ) is the absolute difference between its value on the present mesh and the next coarser mesh, divided by the present mesh value and expressed as a percentage.

Additionally, a comparison of heat dissipation rates obtained with different mesh sizes is shown in Figure 3.

Table 3. Numerically obtained heat dissipation rates, heat transfer coefficients, and average heat sink surface temperatures with respective relative errors for analyzed mesh sizes.

Mesh	Cells, $\times 10^6$	$\dot{Q}$, W	$\delta\dot{Q}$, %	h, W/(m^2·K)	δh,%	$\overline{T}_S$, °C	$\delta\overline{T}_S$, K
M1	0.526	9.618	N/A	5.643	N/A	49.8247	N/A
M2	1.22	9.451	1.76	5.544	1.78	49.829	0.0043
M3	4.12	9.347	1.11	5.482	1.14	49.8329	0.0039
M4	8.969	9.287	0.64	5.446	0.66	49.8349	0.002

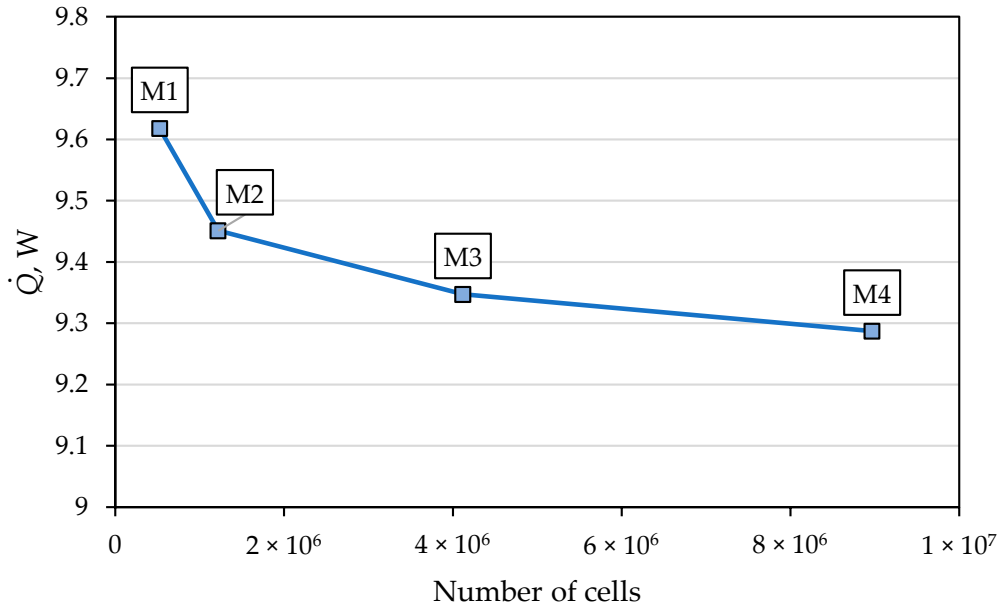


Figure 3. Variation in heat dissipation rate for investigated mesh sizes (M1–M4).

As shown in Table 3 and Figure 3, the obtained quantities vary only slightly with refinement. Between the two finest meshes, M3 and M4, the changes are 0.64% in $\dot{Q}$, 0.66% in h, and 0.002 K in $\overline{T}_S$. Because the variations are negligible, the solution is treated as mesh independent, and the 4.12 million cell mesh (M3) is used for all subsequent simulations. The adopted mesh configuration is presented in Figure 4.

For every analyzed case, it was verified that the specific heat flux at the isothermal base, the sum of specific heat fluxes on all air-exposed solid surfaces, and the net enthalpy flux across the far-field openings (pressure inlet and outlets) agree within 0.1%.

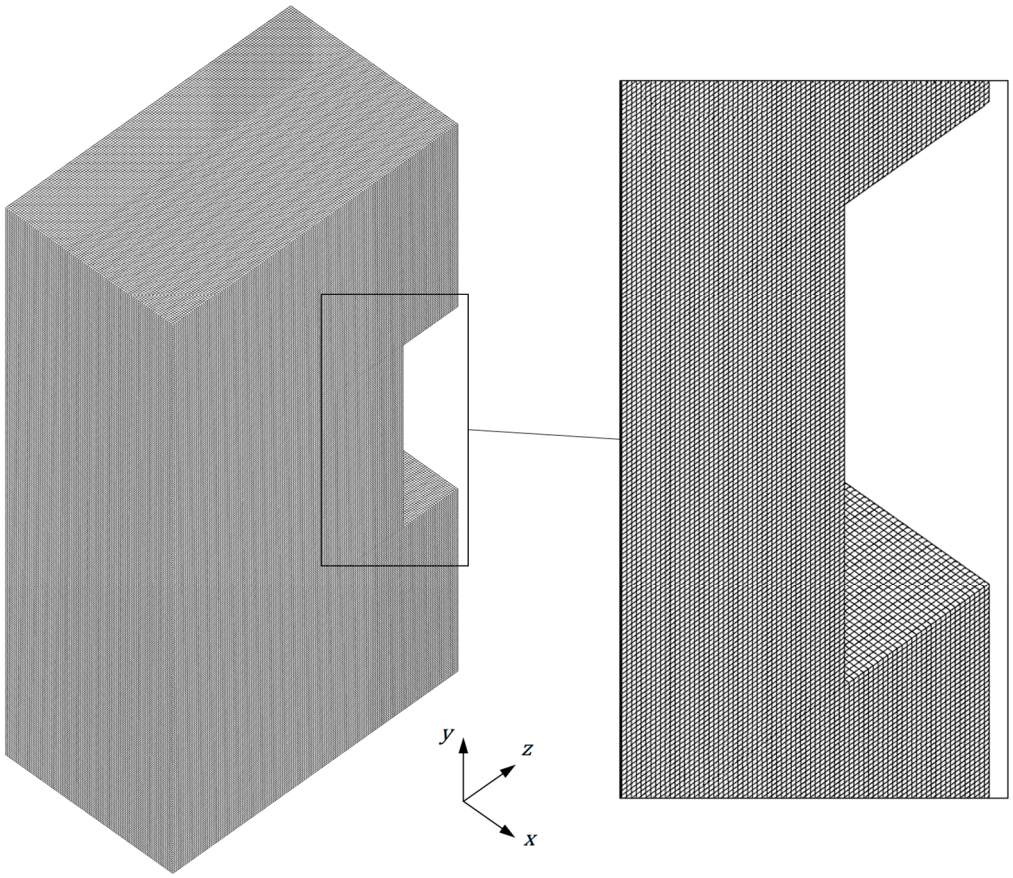


Figure 4. Adopted mesh configuration and close-up of the heat sink region.

3. Experimental Validation

In order to assess the validity of the mathematical model and numerical procedure, numerically obtained heat dissipation rates and heat transfer coefficients have been compared against those obtained experimentally using a purpose-built experimental apparatus.

3.1. Experimental Apparatus

For the purpose of experimental validation, an experimental test heat sink, with geometric characteristics corresponding to those described in Table 1, has been tested in laboratory conditions through a series of calorimetric experiments. Because only natural convection heat transfer is included in the numerical treatment, a polished aluminum heat sink is used to minimize the effects of radiation.

To replicate the thermal load on an electronic component, a tin vessel was filled with water of known mass and used as the heat source. The heat sink was rigidly mounted on one side of the vessel, with its base coated in a thin, uniform layer of silicone thermal paste to minimize contact resistance [31]. To suppress environmental heat losses, all vessel faces except the contact surface were insulated with 25 mm of expanded rubber foam and additionally covered with aluminum foil to reduce radiative heat transfer. The experimental apparatus, both as a schematic and constructed, is shown in Figure 5.

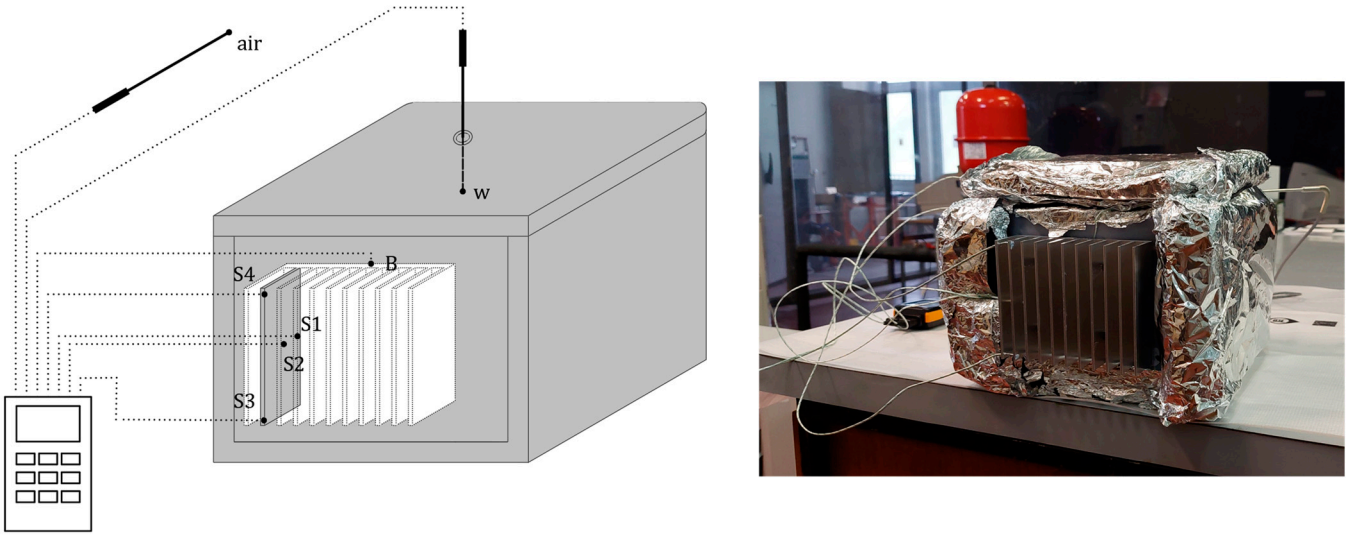


Figure 5. Experimental apparatus with temperature sensor positions at the heat sink base (B) and fin surface (S1–S4): schematic (**left**) and constructed (**right**).

3.2. Experimental Procedure

The experiment began once water at a uniform initial temperature was poured into the vessel. During the initial transient stage, the heat sink and vessel walls warmed as heat was transferred from the water, while the bulk water temperature dropped. After this unsteady period, the system entered a quasi-steady regime in which the water temperature decreased at an approximately linear rate and heat sink surface temperatures displayed only small variations.

Temperatures were monitored continuously throughout the test at 1 s intervals. Water bulk temperature was monitored with a thermistor probe immersed at the vessel center (accuracy ± 0.02 °C), as was the temperature of the surrounding air. In order to track transient thermal response at characteristic points of the heat sink surfaces, four K-type thermocouples (accuracy ± 0.2 °C) were installed along the width and height of a representative inner fin surface and one thermocouple was installed between the heat sink base and the water vessel. Table 4 lists the thermocouple locations on the representative fin as offsets; L is the vertical distance from the fin bottom and H is the horizontal distance from the base–fin junction.

Table 4. Surface thermocouple positions on the heat sink fin and their identifiers.

Measurement Position		Thermocouple Identifier
***L*, mm**	***H*, mm**	
50	1	S1
50	15	S2
1	29	S3
99	29	S4

The experimentally obtained heat dissipation rate was calculated through the following expression:

$$\dot{Q} = \frac{m_w c_w \Delta T_w}{\tau} \tag{26}$$

In Equation (26), m_w is the mass of water inside the vessel (kg), c_w is the specific heat capacity of water (J/(kg·K)), ΔT_w is the change in water bulk temperature during the quasi-steady period (°C), and τ is the duration of the quasi-steady period (s).

The experimentally obtained heat transfer coefficient was obtained in the following way:

$$h = \frac{\dot{Q}}{A_S(\overline{T}_S - T_{air})} \tag{27}$$

In Equation (27), A_S is the surface area of the heat sink in contact with the surrounding air (m^2), $\overline{T_S}$ is the average surface temperature on the surface A_S, obtained as the arithmetic mean of fin temperatures obtained with thermocouples S1–S4 (°C), and T_{air} is the measured ambient air temperature (°C). The surface area A_S is calculated as:

$$A_S = 2nHL + 2nHt + nLt + 2Lb + 2Wb + (n-1)Ls \tag{28}$$

As seen from Equation (28), A_S includes the two side faces of every fin ($2nHL$), the exposed fin end faces at top and bottom of the array ($2nHt$), the fin tips (nLt), the vertical and horizontal faces of the base that are open to air ($2Lb$ and $2Wb$), and the base top strips between fins, $(n-1)Ls$. Substituting the dimensions from Table 1 into Equation (28) yields a total exposed surface area of 0.082 m^2.

A total of three experiments were performed, with different initial temperatures of water in each investigation. In all experiments, the mass of water was equal at 3.467 kg (scale accuracy ±0.005 kg), as was the duration of the quasi-state period, 960 s (16 min), with specific heat of water taken as 4184 J/(kg·K).

Uncertainties in the heat dissipation rate ($\dot{Q}$) and the heat transfer coefficient (h) were evaluated using a straightforward propagation of errors approach, as described by Kline–McClintock [32] and Moffat [33]. In the uncertainty evaluation, the heat sink surface area and time were taken as exact and the surface temperature was taken as the average of four thermocouples. Combined with the declared accuracies of measurement instruments, and using ±2.09 J/(kg·K) for specific heat capacity uncertainty, the relative uncertainties for the heat dissipation rate are 5.2%, 3.3%, and 2.1% for experiments 1, 2 and 3, respectively, while the relative uncertainties for the heat transfer coefficient are 5.3%, 3.3%, and 2.1% for the same measurements.

Although the analyzed heat sink is polished, uncoated aluminum (with emissivity ε of approximately 0.05), for which prior studies consider radiative exchange to be secondary at the present temperatures, its contribution to the total heat dissipation rate and to the heat transfer coefficient can be estimated using the Stefan–Boltzmann relations ($\sigma = 5.67 \times 10^{-8}$ W/(m^2·K^4)):

$$\dot{Q}_r = \varepsilon\sigma\left(\overline{T}_S^4 - T_{air}^4\right)A_S \tag{29}$$

$$h_r = \frac{\varepsilon\sigma\left(\overline{T}_S^4 - T_{air}^4\right)}{\overline{T}_S - T_{air}} \tag{30}$$

For the present operating conditions, $\dot{Q}_r$ lies between 0.37 and 0.91 W and h_r between 0.33 and 0.36 W/(m^2·K), corresponding to 6.2–6.5% of the total heat dissipation rate and of the heat transfer coefficient, respectively. These fractions, consistent with the literature for low-emissivity aluminum at similar temperatures, are an order of magnitude smaller than their convective counterparts. Accordingly, radiation is neglected, and the heat sink heat dissipation is treated as convection-only throughout the experimental data reduction.

3.3. Comparison of Results

A representative run of an experimental measurement (experiment 2), with sampled water (w) and ambient (air) temperatures, as well as heat sink temperatures at the base (B) and at the heat sink surface (S1, S2, S3, S4), is shown in Figure 6.

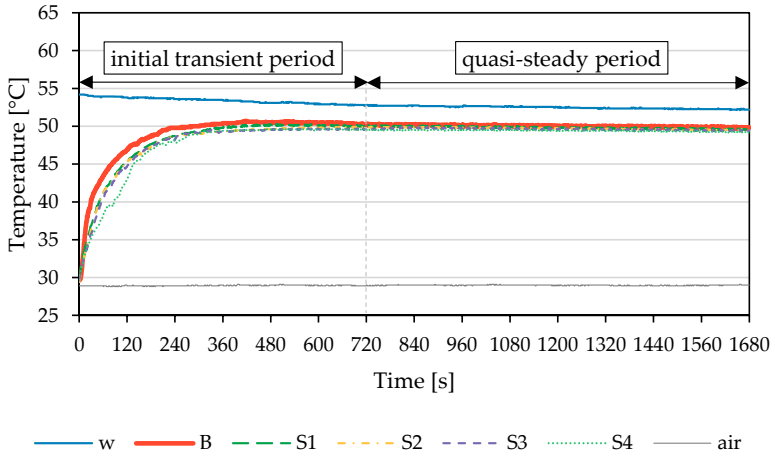


Figure 6. Representative run of an experimental measurement, with water, base, fin surfaces, and ambient air temperatures over time.

As seen from Figure 6, after the initial unsteadiness, the bulk water temperature decreases almost linearly, and the four surface thermocouples remain within a narrow band throughout the quasi-steady interval. The ambient temperature is essentially unchanged over the entire measurement. Heat sink base and surface temperatures were averaged along the quasi-steady period between times 720 and 1680 s, i.e., 12 and 28 min. A 16 min window was used in all three experiments to ensure consistent statistics and fair comparison. The window start/end were chosen by simple stability checks: the base temperature slope was small and nearly linear, the surface temperature varied only slightly, and the ambient air was essentially constant. At the start and at the end of the quasi-steady period, the water bulk temperature difference was obtained in order to calculate the average heat dissipation rate, as well as the heat transfer coefficient.

During the quasi-steady period, the heat sink base temperature decreased by about 0.4 °C, the surface varied by up to 0.3 °C, and the water temperature dropped by 0.38–0.96 °C, while ambient air was essentially at constant temperature. Using standard laminar natural convection scaling, these small drifts correspond to a maximum change of approximately 0.4% in the heat transfer coefficient and approximately 2% in total heat dissipation rate, suggesting negligible variation in the two validation quantities during the quasi-steady period.

Averaged values of measured temperatures on the base surface (T_B) and on characteristic fin positions (T_{S1}, T_{S2}, T_{S3}, T_{S4}), as well as of the surrounding ambient air (T_{air}) for all three experiments, are given in Table 5. Also given in the table for each experiment are mean surface temperatures ($\overline{T_S}$), water bulk temperature differences (ΔT_w), as well as derived values of heat dissipation rate ($\dot{Q}$) and heat transfer coefficient (h), combined with their absolute uncertainties.

Table 5. Summary of quasi-steady temperatures and validation metrics for the three experiments.

Measured/Derived Quantity	Experiment 1	Experiment 2	Experiment 3
T_B, °C	42.3	50	59.8
T_{S1}, °C	42.2	49.8	59.5
T_{S2}, °C	42.1	49.7	59.4
T_{S3}, °C	41.9	49.4	59
T_{S4}, °C	42	49.6	59.2
$\overline{T_S}$, °C	42.05	49.63	59.28
ΔT_w, °C	0.38	0.61	0.96
T_{air}, °C	28.39	29.02	28.61
$\dot{Q}$, W	5.74 ± 0.3	9.47 ± 0.3	14.51 ± 0.3
h, W/(m^2·K)	5.13 ± 0.27	5.46 ± 0.18	5.77 ± 0.12

Operating conditions, i.e., ambient and heat sink base temperatures used in numerical calculations, corresponded to those in the performed experiments. Because the film temperatures across all validation cases lie within a narrow band (between approximately 35 and 45 °C), a single set of thermophysical properties (as given in Table 2) was used for all validation cases.

A comparison of numerically and experimentally obtained heat dissipation rates for different base temperatures in the performed cases is given in Figure 7.

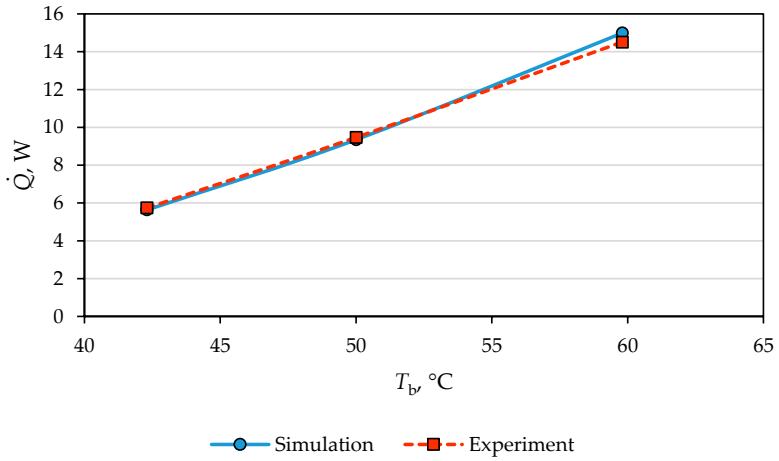


Figure 7. Comparison of heat dissipation rates derived from numerical simulations and experimental measurements.

As shown in Figure 7, the numerically predicted heat dissipation rates agree very well with those calculated from the experimental measurements across all three base temperatures. As the heat sink base temperature increases from 42.3 to 50, and finally to 59.8 °C, the numerical results track the experimentally obtained rise in heat dissipation rate. For base temperatures of 42.3, 50, and 59.8 °C, numerical simulations yield 5.64, 9.34, and 14.99 W, with percentage deviations from the experiment of 1.8%, 1.27%, and 3.32%. This agreement indicates that the governing model and numerical procedure accurately capture the heat transfer process of heat dissipation through a passive heat sink.

Using numerically obtained heat dissipation rates and average temperatures of the heat sink surface in contact with the ambient air, heat transfer coefficients can be obtained ac-

cording to Equation (27). In addition to the experimental data, the heat transfer coefficients are compared with values calculated from an empirical Nusselt number correlation:

$$h = \frac{\mathrm{Nu_s} \cdot k_{\mathrm{air}}}{s} \tag{31}$$

An empirical correlation proposed by Bar-Cohen and Rohsenow [4] provides the following expression to calculate the Nusselt number for symmetric isothermal plates:

$$\mathrm{Nu_s} = \left[\frac{576}{(\mathrm{Ra_s} s/L)^2} + \frac{2.873}{(\mathrm{Ra_s} s/L)^{0.5}} \right]^{-0.5} \tag{32}$$

The Rayleigh number can be obtained in the following way:

$$\mathrm{Ra_s} = \frac{g \beta_{\mathrm{air}} \rho_{\mathrm{air}}^2 c_{\mathrm{p,air}} (\overline{T}_{\mathrm{S}} - T_{\mathrm{air}}) s^3}{\mu_{\mathrm{air}} k_{\mathrm{air}}} \tag{33}$$

In Figure 8, numerically obtained heat transfer coefficients are compared with experimental results and values derived from the used empirical correlation for different base temperatures in the considered cases.

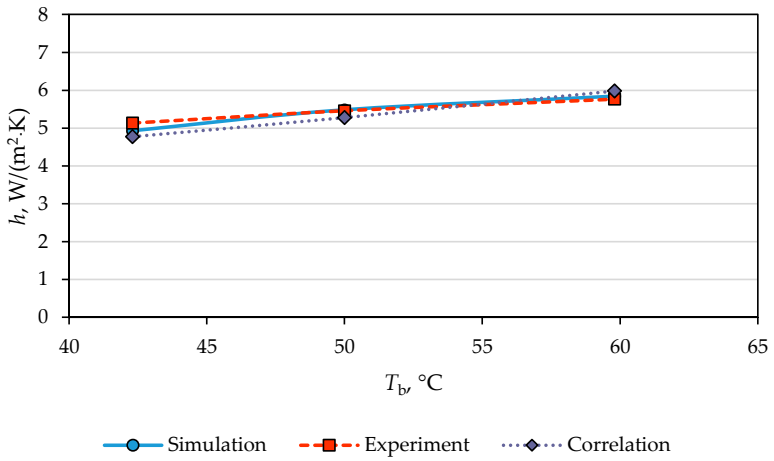


Figure 8. Comparison of heat transfer coefficients derived from numerical simulations, experimental measurements, and the Bar-Cohen–Rohsenow correlation [4].

Figure 8 shows very good agreement among the numerically predicted, experimentally measured, and correlation-based heat transfer coefficients across the selected range of base temperatures. For base temperatures of 42.3, 50, and 59.8 °C, numerical simulations predict 4.93, 5.48, and 5.84 W/(m^2·K), with percentage deviations from the experimentally derived heat transfer coefficients of 3.98%, 0.37%, and 1.29%. Thus, the observed deviations are encompassed by the combined experimental, numerical, and correlation uncertainties. Taken together, the agreement across methods provides further evidence that the used model and numerical setup adequately describe the heat sink heat transfer phenomena and can be used to perform further numerical analyses.

4. Numerical Analysis and Physical Interpretation

4.1. Definition of Analysis Parameters and Performance Metrics

Numerical analyses have been performed to assess the influence of a heat sink's geometry on its thermal performance. Heat sink geometry was varied using two nondimensional

geometric parameters in order to generalize the results beyond the specific fin dimensions. The first parameter is the fin spacing-to-thickness ratio, defined as:

$$S^* = \frac{s}{t} \tag{34}$$

In the analysis, the fin number and spacing were varied such that the overall width W and length L were held constant, thereby maintaining a constant base area. The fin thickness was fixed at 3 mm across all the examined configurations. Similarly, all other geometric parameters correspond to those given for the baseline configuration. Table 6 lists the investigated values of S^*, along with corresponding fin numbers n and fin spacings s. For the investigated configurations in this analysis, the modified Rayleigh number based on fin spacing (Ra_s) is between 293 and 5064, which lies within the canonical laminar range for natural convection between vertical parallel plates.

Table 6. Analyzed fin spacing-to-thickness ratios and corresponding fin numbers and spacings.

Case	$S^* = s/t$, –	n, –	s, mm
1	1.86	15	5.57
2	2.08	14	6.23
3	2.33	13	7
4	2.64	12	7.91
5	3	11	9
6	3.44	10	10.33
7	4	9	12
8	4.8	8	14.4

The second investigated parameter is the fin height-to-spacing ratio (H^*), defined as:

$$H^* = \frac{H}{s} \tag{35}$$

In this analysis, only fin height H was varied, while all other geometric parameters were fixed at values given in Table 1. The heat sink mass m (kg) is listed for reference, because, in a separate trade-off study, mass-specific heat dissipation rate was evaluated. The examined values of H^*, together with corresponding fin heights H and heat sink masses (m), are given in Table 7.

Table 7. Analyzed fin height-to-spacing ratios and corresponding fin heights.

Case	$H^* = H/s$, –	H, mm	m, kg
1	1.11	10	0.2904
2	2.22	20	0.3801
3	3.33	30	0.4698
4	4.44	40	0.5596
5	5.56	50	0.6493
6	6.67	60	0.739
7	7.78	70	0.8288

In the analyses, heat sink thermal performance was assessed based on the following performance metrics:

- Heat dissipation rate $\dot{Q}$
- Heat transfer coefficient h.
- Overall thermal resistance R (K/W), defined as the temperature difference between the heat sink base and ambient air temperature divided by the heat dissipation rate:

$$R = \frac{T_b - T_{air}}{\dot{Q}} \quad (36)$$

- Fin efficiency η, defined as:

$$\eta = \frac{\tanh(mH_c)}{mH_c} \quad (37)$$

where

$$m = \sqrt{\frac{2h}{k_{Al}t}} \quad (38)$$

In Equation (37), H_c is the effective fin height accounting for tip convection [34], calculated as:

$$H_c = H + \frac{t}{2} \quad (39)$$

In Equations (37) and (38), m (–) is the fin parameter that compares convection on the fin surface with conduction along the fin, calculated using the heat transfer coefficient h, fin material conductivity k_{Al}, and fin thickness t.

In both performed analyses, the base temperature was held constant at 50 °C and the ambient air temperature was 29 °C.

4.2. Analysis of the Influence of Fin Spacing-to-Thickness Ratio

The influence of S^* on each of the selected performance metrics is evaluated for the baseline fin height, i.e., for H^* = 3.33, and presented graphically in the following section. Additionally, representative temperature contours and velocity vectors are shown to aid interpretation and illustrate how variation in S^* influences the underlying heat dissipation mechanisms.

Figure 9 shows the influence of S^* on the heat dissipation rate.

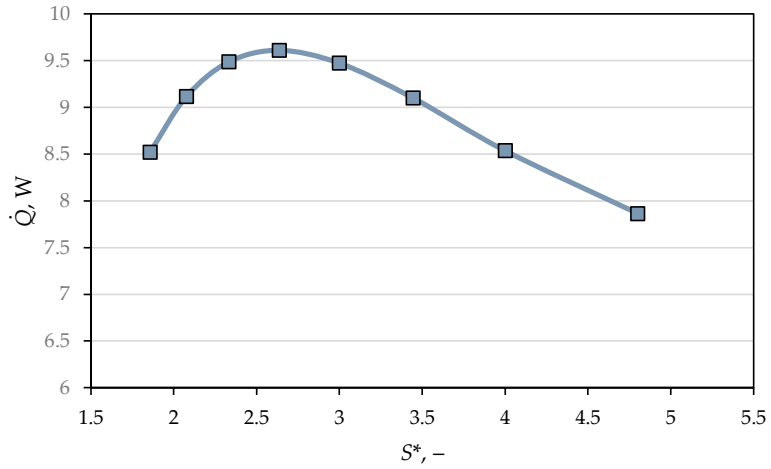


Figure 9. Influence of fin spacing-to-thickness ratio on heat dissipation rate.

As can be seen from Figure 9, the heat dissipation rate initially increases with increasing S^*, reaches a peak, and then declines as S^* continues to rise. This trend indicates an optimal spacing ratio at an S^* value of approximately 2.6, where the combination of enhanced airflow and sufficient total heat transfer area yields maximum heat transfer. At low S^*, fins are densely packed, leading to restricted airflow, increased thermal resistance on the air side, and reduced convection. As fins are spaced further apart, convection improves until the reduction in the total number of fins (and thus total surface area) begins to dominate, causing $\dot{Q}$ to drop.

The influence of S^* on the heat transfer coefficient is shown in Figure 10.

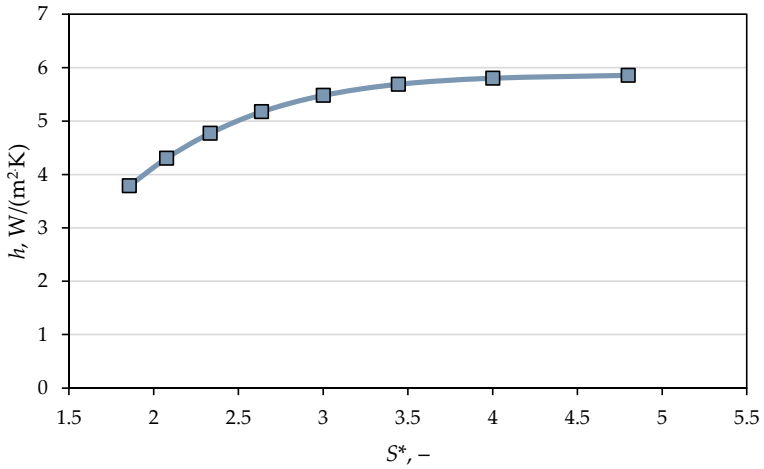


Figure 10. Influence of fin spacing-to-thickness ratio on the heat transfer coefficient.

It can be observed from Figure 10 that the heat transfer coefficient h rises sharply with increasing S^* at first and then subsides. The initial rise results from improved airflow between fins as spacing increases, developing more effective convective heat transfer at the fin surfaces. As the effect of further increasing spacing reaches a plateau, gains in h become limited, reflecting the diminishing returns once airflow is no longer significantly hindered.

The influence of S^* on the overall thermal resistance is given in Figure 11.

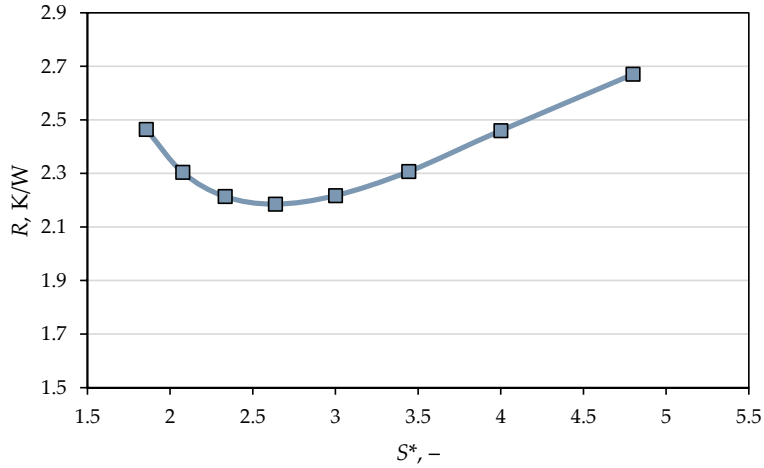


Figure 11. Influence of fin spacing-to-thickness ratio on the overall thermal resistance.

Figure 11 indicates that overall thermal resistance R exhibits a non-monotonic trend, with a minimum, i.e., optimal point, corresponding roughly to the maximum of $\dot{Q}$. At small spacings, overall thermal resistance is high due to poor airflow and less effective heat transfer. As spacing increases to an optimal value, R reaches its lowest point and heat transfer is maximized. For even larger S^*, R increases as the total fin surface area decreases and less heat is conducted away.

Figure 12 shows the influence of S^* on fin efficiency.

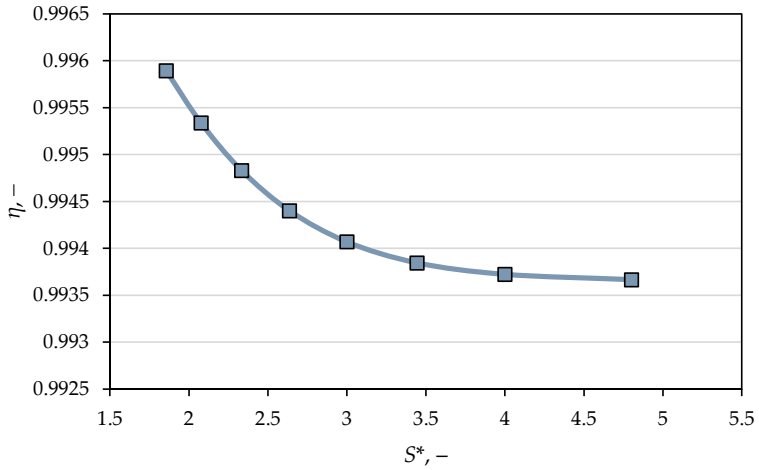


Figure 12. Influence of fin spacing-to-thickness ratio on fin efficiency.

As can be observed from Figure 12, fin efficiency η declines gently with increasing S^*, though the variation is small. At low S^*, heat is spread over a greater number of closely packed fins, so individual fins dissipate less heat and operate with higher efficiency, i.e., the temperature drop along the fin is smaller. As fins become more widely spaced, each fin carries a greater portion of the thermal load, making the temperature gradient along the fin more pronounced and reducing efficiency.

As seen from Figures 9–12, the most favorable considered fin spacing-to-thickness ratio with respect to heat dissipation rate and overall thermal resistance, while also avoiding diminishing returns in the heat transfer coefficient and fin efficiency, is 2.64, corresponding to a fin spacing of 7.91 mm. For reference, this is compared with the expression for thermally optimum fin spacing for vertical parallel plates provided by Bar-Cohen and Rohsenow [4]:

$$s_{\text{opt}} = \frac{2.714L}{\text{Ra}_{\text{L}}} \tag{40}$$

Substituting the values of L (as provided in Table 1) and Ra_{L} (calculated as shown in Equation (1)) yields an optimum fin spacing of 7.52 mm. As is evident, there is a clear agreement between these values, with a discrepancy of 5.2%. A certain deviation is expected because the classical result assumes zero thickness, infinitely wide, isothermal plates, while the investigated heat sink configuration has a finite array of fins, finite thickness, three-dimensional end/tip effects, and non-isothermal fins (finite fin efficiency). The close agreement supports the consistency of the present results with established theory.

In addition to the performance curves, temperature contours and velocity vector maps are presented on the fins' mid-height plane, which throughout this analysis corresponds to a plane 15 mm above the air-exposed base surface. Alongside the most favorable case (S^* = 2.64), the lower and upper bounds of the explored S^* range are included to bracket the optimum. To visualize the underlying physics, Figure 13 presents the fins' mid-height temperature contours and Figure 14 shows velocity vectors for fin spacing-to-thickness ratios of 1.86 (s = 5.57 mm, n = 15), 2.64 (s = 7.91 mm, n = 12), and 4.8 (s = 14.4 mm, n = 8) at fixed H^* = 3.33.

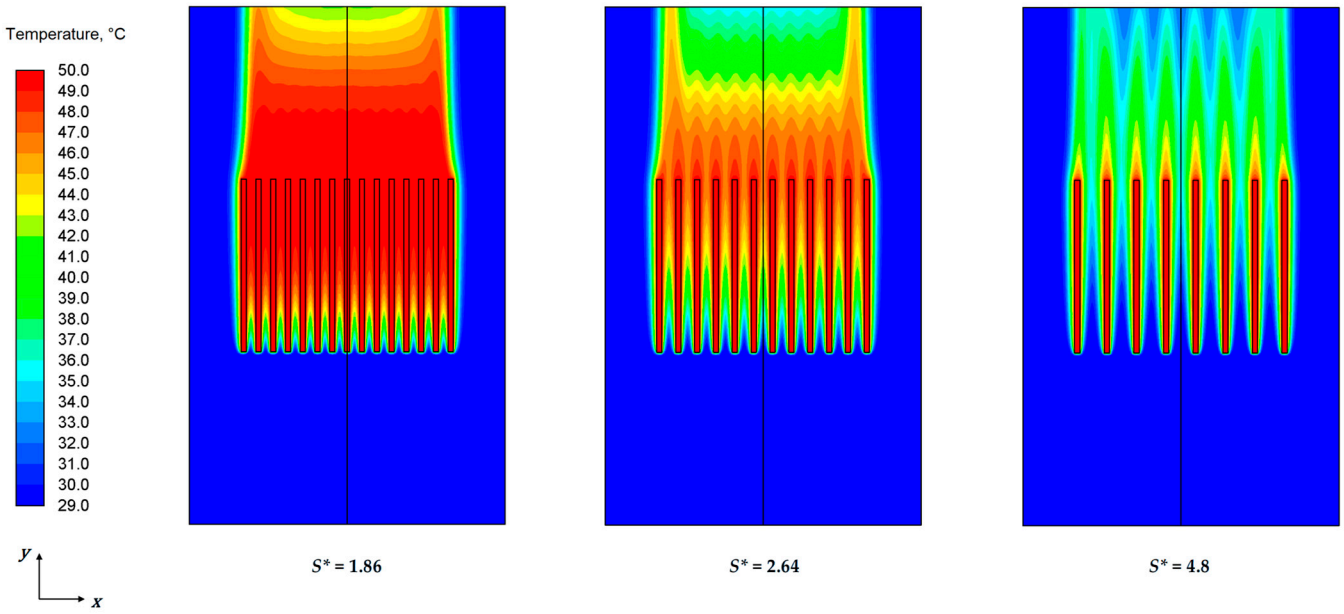


Figure 13. Temperature contours in the fins' mid-height plane (H = 15 mm) for fin spacing-to-thickness ratios of 1.86, 2.64, and 4.8 at H^* = 3.33.

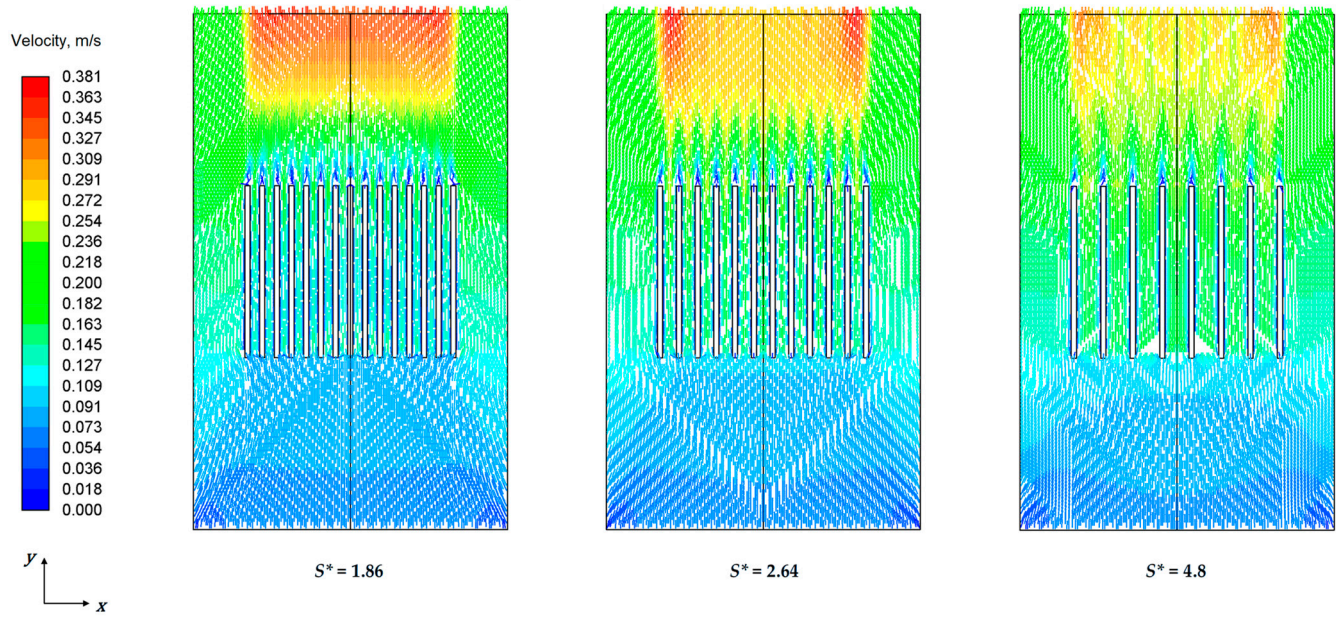


Figure 14. Velocity vectors in the fins' mid-height plane (H = 15 mm) for fin spacing-to-thickness ratios of 1.86, 2.64, and 4.8 at H^* = 3.33.

The mid-height (H = 15 mm) fields in Figures 13 and 14 highlight the balance between adding fin surface and preserving open passage for buoyancy-driven inflow. At tight spacing (S^* = 1.86), opposing wall boundary layers merge well below fin mid-length, which throttles the inter-fin throughflow; the slice shows a broad, warm core above the array and muted vertical velocities within the slots. Near the optimal spacing (S^* = 2.64), the slots remain open and a single, continuous buoyant plume forms: the mid-height slots are cooler than at tight spacing, and the wall-normal temperature gradients are steeper because the boundary layers remain distinct and relatively thin up to approximately mid-length. At wide spacing (S^* = 4.8), the mid-height slot is the coolest of the three cases due to easier ambient access. However, the total fin surface area is substantially reduced, and the boundary layers thicken by mid-length, so wall gradients weaken and the plume breaks

into diffuse branches with increased side bypass in the end slots. Consequently, despite a colder slot core at $S^* = 4.8$, the array dissipates less heat and exhibits higher thermal resistance, whereas $S^* = 2.6$ delivers the best overall performance by combining adequate area with sustained inter-fin convection.

4.3. Analysis of the Influence of Fin Height-to-Spacing Ratio

The effect of H^* on chosen performance metrics is assessed for the baseline fin spacing, i.e., for $S^* = 3$, and shown graphically in this section. Also, representative temperature contours and velocity vector maps are included to aid interpretation and show how changes in H^* modify the underlying heat dissipation mechanisms.

The dependence of the heat dissipation rate on H^* is shown in Figure 15.

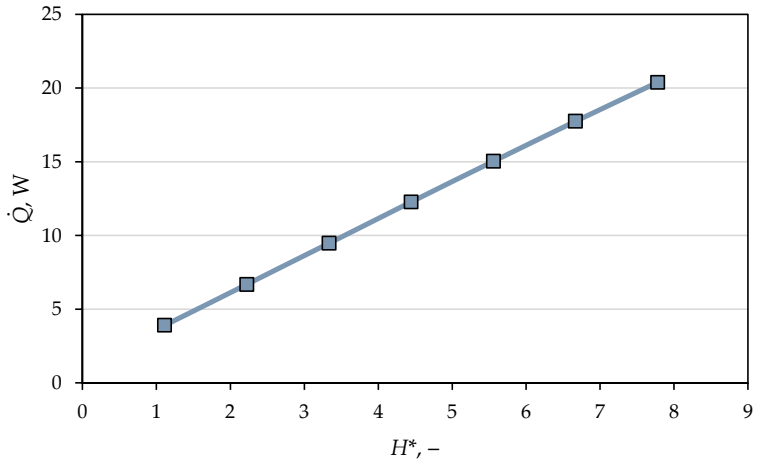


Figure 15. Influence of fin height-to-spacing ratio on heat dissipation rate.

As seen from Figure 15, the heat dissipation rate $\dot{Q}$ increases nearly linearly with H^*. Increasing fin height for fixed spacing and base area directly adds to exposed surface area and thus increases heat dissipation. While increasing fin surface area invariably enhances heat dissipation rate, it also increases the heat sink's volume and mass and thus its cost. To capture this trade-off, the mass-specific heat dissipation rate has been evaluated as a function of H^* and the results are shown in Figure 16.

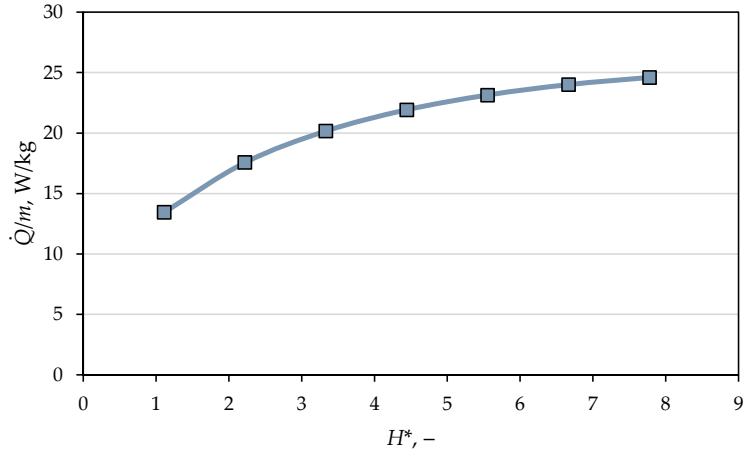


Figure 16. Influence of fin height-to-spacing ratio on mass-specific heat dissipation rate.

The ratio $\dot{Q}/m$, representing heat dissipation per unit mass, shows a nonlinear trend with diminishing returns, as shown in Figure 16. $\dot{Q}/m$ increases quickly at lower H^* and then plateaus at higher values, indicating that adding height initially raises cooling

efficiency per unit mass but becomes progressively less effective as each additional unit of mass contributes a smaller increment to total heat dissipation. This metric could be valuable for lightweight thermal management, where maximizing efficiency with minimal mass is important.

The influence of H^* on the heat transfer coefficient is given in Figure 17.

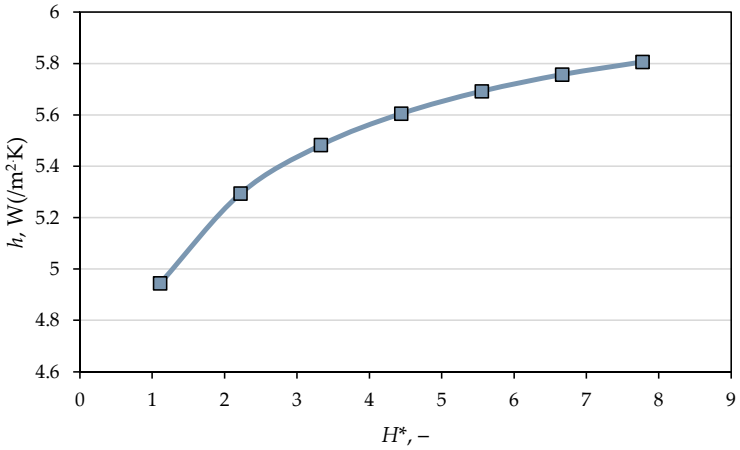


Figure 17. Influence of fin height-to-spacing ratio on the heat transfer coefficient.

The heat transfer coefficient h increases slowly as H^* grows, but the rise is less pronounced than for $\dot{Q}$. Increasing fin height does not extend the convective development length, but only the slot depth, as h is governed mainly by fin spacing and length. The airflow through the slots is essentially two-dimensional, so increasing H^* above approximately 3 does not result in significant heat transfer coefficient enhancement.

Figure 18 shows the influence of H^* on the overall thermal resistance.

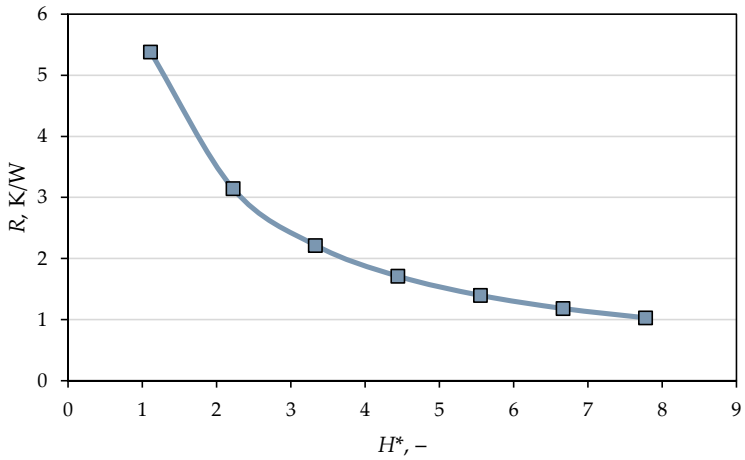


Figure 18. Influence of fin height-to-spacing ratio on the overall thermal resistance.

As seen from Figure 18, thermal resistance R decreases continuously as H^* increases. Taller fins reduce resistance to heat flow as a result of the increased heat dissipation rate due to their greater surface area. The drop is steepest at lower H^*, again pointing to diminishing returns for increasing fin height; after a certain point, additional height provides smaller improvements.

The influence of H^* on fin efficiency is shown in Figure 19.

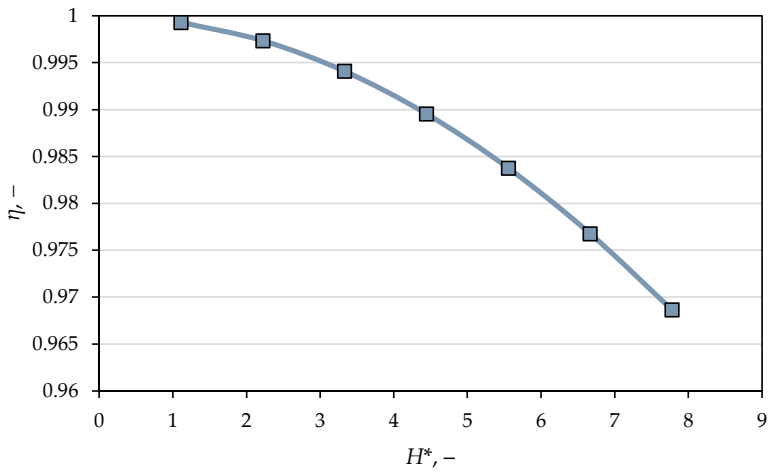


Figure 19. Influence of fin height-to-spacing ratio on fin efficiency.

Fin efficiency η declines steadily as H^* increases, as seen from Figure 19. This is expected as greater height increases the internal temperature drop within each fin, making it harder for the entire fin to efficiently contribute to heat transfer. The effect is more noticeable at higher ratios, reflecting the conduction limit relative to the additional surface area.

As shown in the corresponding performance plots, the heat dissipation rate increases and the overall thermal resistance decreases with H^*, with diminishing returns at the upper end of the range for the latter. To visualize the underlying physics beyond the performance curves, temperature contours and velocity vector maps are presented on the normalized fins mid-height plane (z/H = 0.5) for fin height-to-spacing ratios of 1.11 (H = 10 mm), 4.44 (H = 40 mm), and 7.78 (H = 70 mm) at fixed S^* = 3. Because H varies in this analysis, the absolute plane height changes accordingly: the plane lies 5 mm, 20 mm, and 35 mm from the air-exposed base surface for H = 10, 40, and 70 mm, respectively. Figure 20 presents temperature contours and Figure 21 shows velocity vector maps at z/H = 0.5.

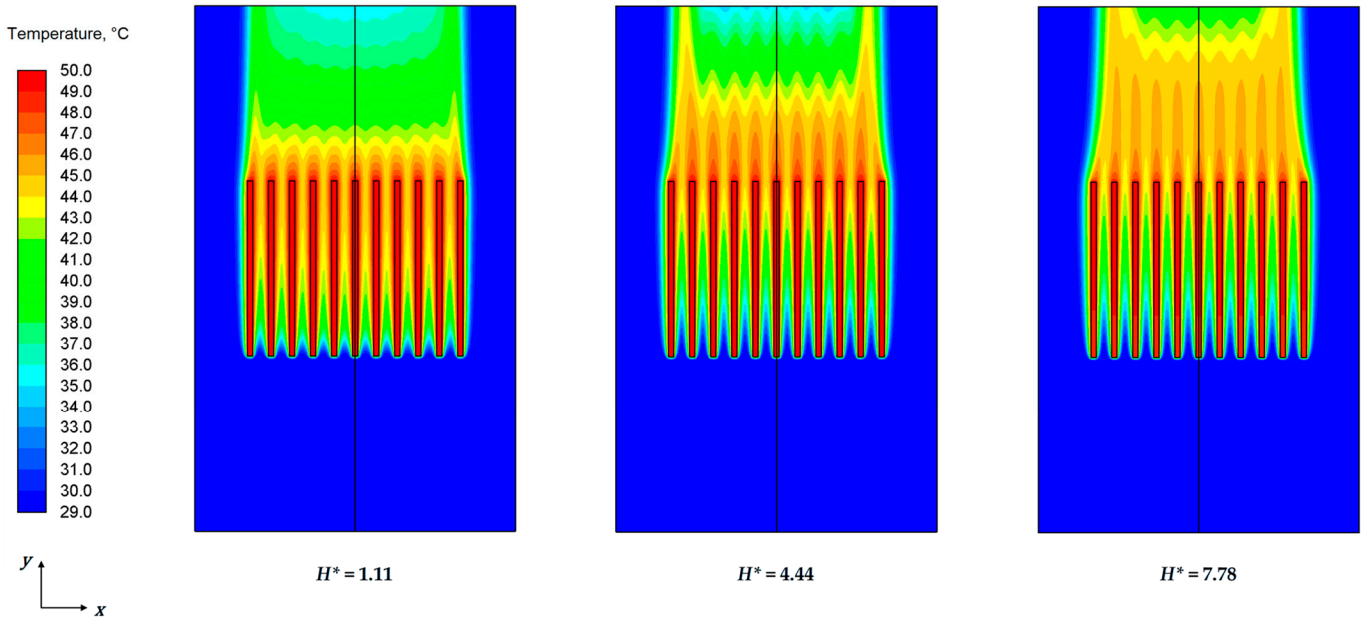


Figure 20. Temperature contours in the normalized fins' mid-height plane (z/H = 0.5) for fin height-to-spacing ratios of 1.11, 4.44, and 7.78 at S^* = 3.

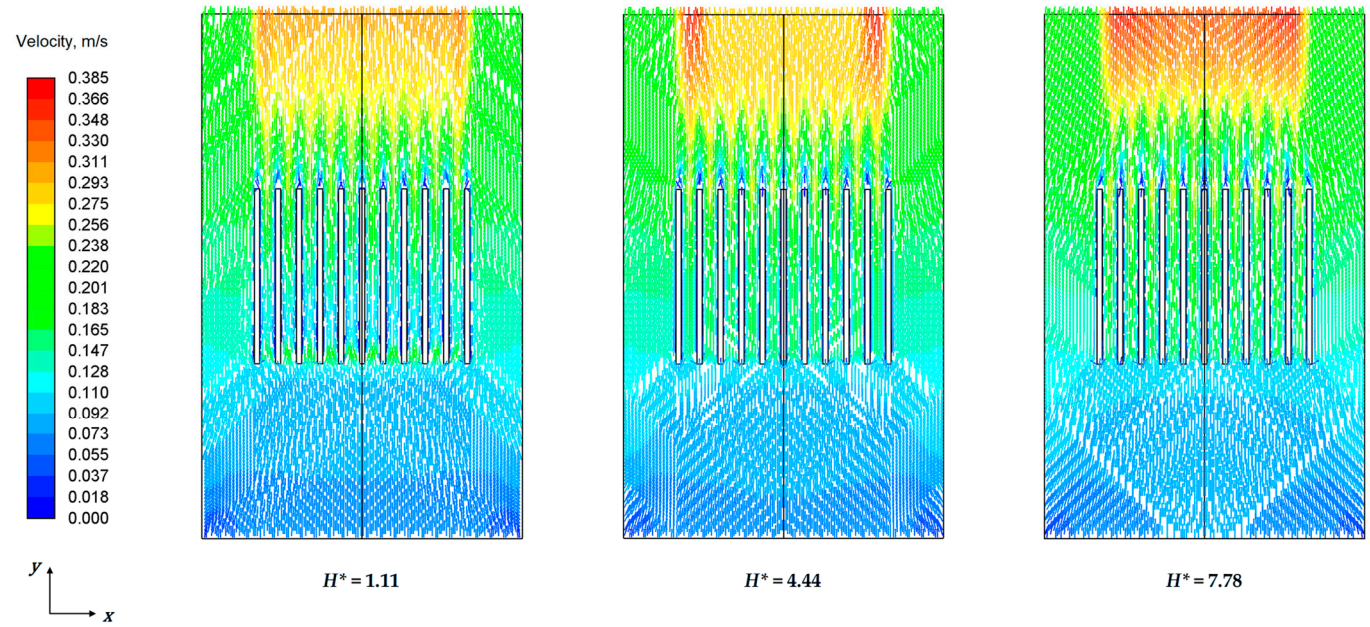


Figure 21. Velocity vectors in the normalized fins' mid-height plane (z/H = 0.5) for fin height-to-spacing ratios of 1.11, 4.44, and 7.78 at S^* = 3.

The fins' mid-height plane (z/H = 0.5) fields in Figures 20 and 21 show how increasing fin height raises total heated area and strengthens the core updraft but with diminishing returns once wall temperatures fall and boundary layers thicken. At H^* = 1.11, the slots supply a limited heated surface, so the upward velocities in the slots are modest and mid-height slots remain warm. The near-wall thermal layers are thin and well separated, but the small total area limits throughflow and heat removal. At H^* = 4.44, the added sidewall area injects more buoyant momentum into the slots, resulting in a more intense buoyant plume. Additionally, mid-height slot temperatures are noticeably lower, and the boundary layers remain distinct at this plane, maintaining steeper wall-normal temperature gradients and higher local heat fluxes. At H^* = 7.78, total heat dissipation area increases further, but the incremental cooling at the fins' mid-height plane is smaller. Furthermore, fin surfaces are cooler as the local temperature difference is lower due to fin-efficiency limits. The thermal layers are thicker by z/H = 0.5, and the wall gradients weaken, so the added area is used less effectively. Consequently, heat dissipation rate increases with H^* while the heat transfer coefficient grows sublinearly, and the mass-specific performance tends to level off at high H^*, which is consistent with the diminishing returns trend seen in the performance curves.

4.4. Limitations and Future Directions

This study isolates the first-order geometric effects of $S^* = s/t$ and $H^* = H/s$ for a vertical, buoyancy-driven plate fin heat sink with results representative of laminar natural convection, with Ra_L ranging from 1.13×10^6 and 2.5×10^6 and Ra_s ranging from 293 to 5064.

For the explored range of operating temperatures and heat sink surface characteristics, radiation was found to be a minor share and was therefore neglected.

The heat sink base was assumed to be isothermal due to aluminum's high thermal conductivity, which quickly equalizes lateral temperature across the base, which corresponded well with performed experimental measurements.

Guidance outside these bounds (e.g., different operating temperature range, non-uniform base heating, turbulent/mixed convection, high-emissivity coatings, alternative fin topologies) should be treated cautiously.

Additionally, the base thickness was held fixed at a fixed value throughout the numerical analysis. A thinner base would increase lateral spreading resistance and reduce temperature uniformity at the fin roots, which in turn lowers effective fin efficiency, an effect most pronounced for tall fins (e.g., H^* = 4.8). This would likely soften the gains at large H^* and could shift the practical optimum toward slightly lower H^* (or motivate a thicker base). Quantifying this trade-off is planned in the forthcoming analyses and optimization studies.

Building on the present analysis, future work will:

- Quantify S^*–H^* interaction with a design of experiments (DOE) approach and a multi-objective optimization to maximize the heat sink thermal performance, with a special emphasis on the mass-specific performance;
- Extend the geometry set with additional parameters, e.g., base thickness;
- Examine surface emissivity to include convection–radiation coupling;
- Relax the isothermal base assumption via measured heat flux;
- Probe higher Rayleigh numbers (higher operating temperatures or geometric upscaling) and orientation effects to assess the onset of mixed or transitional regimes.

These extensions will convert the present geometry map into generalizable design guidance with explicit trade-offs among performance, mass, and manufacturability.

5. Conclusions

In the paper, the influence of geometric parameters on the thermal performance of a passive vertical aluminum plate fin heat sink under natural convection was studied. In order to generalize the results, two nondimensional geometric parameters were introduced: fin spacing-to-thickness ratio (S^*) and fin height-to-spacing ratio (H^*). S^* was varied in the 1.86 to 4.8 range, while H^* was examined in the 1.11 to 7.78 range. Heat dissipation rate ($\dot{Q}$), heat transfer coefficient (h), overall thermal resistance (R), and fin efficiency (η) were used as performance metrics.

For the fin spacing-to-thickness ratio, the heat dissipation rate was initially observed to increase with greater spacing, reaching a peak value at approximately 2.6 before declining as further spacing reduced the overall heat transfer area. The heat transfer coefficient similarly increased steadily at lower S^* values due to airflow improvement, then began to stagnate, while thermal resistance exhibited a minimum at the optimum spacing, paralleling the heat dissipation rate maximum. Fin efficiency showed a gradual decline with larger S^*, reflecting higher fin utilization at closer spacing.

In contrast, increasing the fin height-to-spacing ratio led to nearly linear improvements in heat dissipation rate but with diminishing returns in the mass-specific heat dissipation rate. The increase in the heat transfer coefficient at higher H^* was milder because increasing fin height deepens the fin channel rather than expanding the convective boundary layer. Overall thermal resistance decreased with the increase in H^*, with the decrease being more prominent at lower H^* values. Fin efficiency exhibited a continuous drop due to increasing temperature gradients within taller fins throughout the investigated H^* range.

The analysis results show a significant influence of investigated parameters on selected performance metrics, providing both the guidelines for selecting favorable geometric parameters and the basis for further numerical analyses and optimization procedures aimed at increasing the thermal performance of passive heat sinks.

Author Contributions: Conceptualization, M.K. and B.D.; methodology, M.K.; software, M.K. and T.F. validation, M.K., T.F. and B.D.; formal analysis, M.K. and T.F.; investigation, M.K., T.F. and B.D.; resources, M.K. and B.D.; data curation, M.K. and T.F.; writing—original draft preparation, M.K. and T.F.; writing—review and editing, M.K., T.F. and B.D.; visualization, M.K. and T.F.; supervision, M.K.

and B.D.; project administration, M.K. and B.D.; funding acquisition, M.K. and B.D. All authors have read and agreed to the published version of the manuscript.

Funding: This work has been supported by the University of Rijeka under the projects Investigating the potential for the renewal of district heating systems using dynamic simulations (uniri-iskusni-tehnic-23-146) and Investigation of the influence of geometry characteristics on the enhancement of latent thermal energy storage thermal efficiency (uniri-mladi-tehnic-23-8).

Institutional Review Board Statement: Not applicable.

Informed Consent Statement: Not applicable.

Data Availability Statement: The original contributions presented in this study are included in the article. Further inquiries can be directed to the corresponding author.

Conflicts of Interest: The authors declare no conflicts of interest.

References

1. Abbas, E.F. An overview of heat sink technology. *Int. J. Appl. Mech. Eng.* **2024**, *29*, 1–23. [CrossRef]
2. Grochalski, K.; Rukat, W.; Jakubek, B.; Wieczorowski, M.; Słowiński, M.; Sarbinowska, K.; Graboń, W. The influence of geometry, surface texture, and cooling method on the efficiency of heat dissipation through the heat sink—A review. *Materials* **2023**, *16*, 5348. [CrossRef]
3. Elenbaas, W. Heat dissipation of parallel plates by free convection. *Physica* **1942**, *9*, 1–28. [CrossRef]
4. Bar-Cohen, A.; Rohsenow, W.M. Thermally optimum spacing of vertical, natural convection-cooled, parallel plates. *J. Heat Transf.* **1984**, *106*, 116–123. [CrossRef]
5. Meng, X.; Zhu, J.; Wei, X.; Yan, Y. Natural convection heat transfer of a straight-fin heat sink. *Int. J. Heat Mass Transf.* **2018**, *123*, 561–568. [CrossRef]
6. Shen, Q.; Sun, D.; Xu, Y.; Jin, T.; Zhao, X. Orientation effects on natural convection heat dissipation of rectangular fin heat sinks mounted on LEDs. *Int. J. Heat Mass Transf.* **2014**, *75*, 462–469. [CrossRef]
7. Bar-Cohen, A.; Iyengar, M.; Kraus, A.D. Design of optimum plate-fin natural convective heat sinks. *J. Electron. Packag.* **2003**, *125*, 208–216. [CrossRef]
8. Mehrtash, M.; Tari, I. A correlation for natural convection heat transfer from inclined plate-finned heat sinks. *Appl. Therm. Eng.* **2013**, *51*, 1067–1075. [CrossRef]
9. Jeon, D.; Byon, C. Thermal performance of plate fin heat sinks with dual-height fins subject to natural convection. *Int. J. Heat Mass Transf.* **2017**, *113*, 1086–1092. [CrossRef]
10. Huang, X.; Shi, C.; Zhou, J.; Zhang, L.; Xu, Z. Performance analysis and design optimization of heat pipe sink with a variable height fin array under natural convection. *Appl. Therm. Eng.* **2019**, *160*, 113939. [CrossRef]
11. Fuse, H.; Oe, S.; Haga, T. Effects of fin height, base thickness, blackening, emissivity and thermal conductivity on heat dissipation of die-cast aluminum alloy heat sink. *Metals* **2025**, *15*, 696. [CrossRef]
12. Abbas, A.; Wang, C.-C. Augmentation of natural convection heat sink via using displacement design. *Int. J. Heat Mass Transf.* **2020**, *154*, 119757. [CrossRef]
13. Joo, Y.; Kim, S.J. Comparison of thermal performance between plate-fin and pin-fin heat sinks in natural convection. *Int. J. Heat Mass Transf.* **2015**, *83*, 345–356. [CrossRef]
14. Ahmadi, M.; Mostafavi, G.; Bahrami, M. Natural convection from rectangular interrupted fins. *Int. J. Therm. Sci.* **2014**, *82*, 62–71. [CrossRef]
15. Quintino, A.; Cianfrini, M.; Petracci, I.; Spena, V.A.; Corcione, M. Dimensionless correlations for natural convection heat transfer from a pair of vertical staggered plates suspended in free air. *Appl. Sci.* **2021**, *11*, 6511. [CrossRef]
16. McCay, O.; Nimmagadda, R.; Ali, S.M.; Persoons, T. A parametric design study of natural-convection-cooled heat sinks. *Fluids* **2023**, *8*, 234. [CrossRef]
17. Altun, A.H.; Ziylan, O. Experimental investigation of the effects of horizontally oriented vertical sinusoidal wavy fins on heat transfer performance in natural convection. *Int. J. Heat Mass Transf.* **2019**, *139*, 425–431. [CrossRef]
18. Chang, S.-W.; Wu, H.-W.; Guo, D.-Y.; Shi, J.-J.; Chen, T.-H. Heat transfer enhancement of vertical dimpled fin array in natural convection. *Int. J. Heat Mass Transf.* **2017**, *106*, 781–792. [CrossRef]
19. Mousavi, H.; Darzi, A.A.R.; Farhadi, M.; Omidi, M. A novel heat sink design with interrupted, staggered and capped fins. *Int. J. Therm. Sci.* **2018**, *127*, 312–320. [CrossRef]
20. Awasarmol, U.V.; Pise, A.T. An experimental investigation of natural convection heat transfer enhancement from perforated rectangular fin arrays at different inclinations. *Exp. Therm. Fluid Sci.* **2015**, *68*, 145–154. [CrossRef]

21. Feng, S.; Shi, M.; Yan, H.; Sun, S.; Li, F.; Lu, T.J. Natural convection in a cross-fin heat sink. *Appl. Therm. Eng.* **2018**, *132*, 30–37. [CrossRef]
22. Wang, K.; Shi, Y.; Chen, J.; Dai, Y. A biomimetic microchannel heat sink for enhanced thermal performance in chip cooling. *Biomimetics* **2025**, *10*, 459. [CrossRef] [PubMed]
23. Soloveva, O.V.; Solovev, S.A.; Shakurova, R.Z. Numerical study of the thermal and hydraulic characteristics of plate-fin heat sinks. *Processes* **2024**, *12*, 744. [CrossRef]
24. Huang, C.-H.; Chen, W.-Y. A natural convection horizontal straight-fin heat sink design problem to enhance heat dissipation performance. *Int. J. Therm. Sci.* **2022**, *176*, 107540. [CrossRef]
25. Muneeshwaran, M.; Tsai, M.-K.; Wang, C.-C. Heat transfer augmentation of natural convection heat sink through notched fin design. *Int. Commun. Heat Mass Transf.* **2023**, *142*, 106676. [CrossRef]
26. Micheli, L.; Reddy, K.S.; Mallick, T.K. Thermal effectiveness and mass usage of horizontal micro-fins under natural convection. *Appl. Therm. Eng.* **2016**, *97*, 39–47. [CrossRef]
27. El Ghandouri, I.; Maakoul, A.E.; Saadeddine, S.; Meziane, M. Design and numerical investigations of natural convection heat transfer of a new rippling fin shape. *Appl. Therm. Eng.* **2020**, *178*, 115670. [CrossRef]
28. Aihara, T.; Maruyama, S.; Kobayakawa, S. Free convective/radiative heat transfer from pin-fin arrays with a vertical base plate (general representation of heat transfer performance). *Int. J. Heat Mass Transf.* **1990**, *33*, 1223–1232. [CrossRef]
29. Ansys, Inc. *Ansys Fluent Theory Guide (Release 2024 R1). Section: Density—Incompressible Ideal Gas*; Ansys, Inc.: Canonsburg, PA, USA, 2024.
30. Versteeg, H.K.; Malalasekera, W. *An Introduction to Computational Fluid Dynamics: The Finite Volume Method*, 2nd ed.; Pearson: London, UK, 2007.
31. Fadiga, T. Investigation of Heat Transfer Through a Heat Sink. Master's Thesis, University of Rijeka, Faculty of Engineering, Rijeka, Croatia, 2025. (In Croatian)
32. Kline, S.J.; McClintock, F.A. Describing uncertainties in single-sample experiments. *Mech. Eng.* **1953**, *75*, 3–8.
33. Moffat, R.J. Describing the uncertainties in experimental results. *Exp. Therm. Fluid Sci.* **1988**, *1*, 3–17. [CrossRef]
34. Çengel, Y.A.; Ghajar, A.J. *Heat and Mass Transfer: Fundamentals and Applications*, 6th ed.; McGraw-Hill Education: Singapore, 2020.

Disclaimer/Publisher's Note: The statements, opinions and data contained in all publications are solely those of the individual author(s) and contributor(s) and not of MDPI and/or the editor(s). MDPI and/or the editor(s) disclaim responsibility for any injury to people or property resulting from any ideas, methods, instructions or products referred to in the content.